

Orbit determination of the Lunar Reconnaissance Orbiter

Erwan Mazarico · D. D. Rowlands · G. A. Neumann ·
D. E. Smith · M. H. Torrence · F. G. Lemoine ·
M. T. Zuber

Received: 17 March 2011 / Accepted: 13 August 2011
© Springer-Verlag 2011

Abstract We present the results on precision orbit determination from the radio science investigation of the Lunar Reconnaissance Orbiter (LRO) spacecraft. We describe the data, modeling and methods used to achieve position knowledge several times better than the required 50–100 m (in total position), over the period from 13 July 2009 to 31 January 2011. In addition to the near-continuous radiometric tracking data, we include altimetric data from the Lunar Orbiter Laser Altimeter (LOLA) in the form of crossover measurements, and show that they strongly improve the accuracy of the orbit reconstruction (total position overlap differences decrease from ~ 70 m to ~ 23 m). To refine the spacecraft trajectory further, we develop a lunar gravity field by combining the newly acquired LRO data with the historical data. The reprocessing of the spacecraft trajectory with that model shows significantly increased accuracy (~ 20 m with only the radiometric data, and ~ 14 m with the addition of the altimetric crossovers). LOLA topographic maps and calibration data from the Lunar Reconnaissance Orbiter Camera were used to supplement the results of the overlap analysis and demonstrate the trajectory accuracy.

Electronic supplementary material The online version of this article (doi:10.1007/s00190-011-0509-4) contains supplementary material, which is available to authorized users.

E. Mazarico · D. E. Smith · M. T. Zuber
Massachusetts Institute of Technology, Cambridge, USA

E. Mazarico (✉) · D. D. Rowlands · G. A. Neumann ·
D. E. Smith · M. H. Torrence · F. G. Lemoine
NASA Goddard Space Flight Center, Planetary Geodynamics
Laboratory, Greenbelt, USA
e-mail: erwan.m.mazarico@nasa.gov

M. H. Torrence
S.G.T. Inc., Greenbelt, USA

Keywords Moon · Orbit determination · Gravity ·
Altimetric crossover · Geodesy

1 Introduction

1.1 Objectives

The Lunar Reconnaissance Orbiter (LRO) mission (Chin et al. 2007) was designed to provide a comprehensive (global) and detailed (high-resolution) survey of the Moon, in anticipation of the needs of future orbital and landed exploration missions. The payload consists of seven instruments (Vondrak et al. 2010), some of which have very high spatial resolution: better than 50 cm for the Lunar Reconnaissance Orbiter Camera (LROC) system (Robinson et al. 2010), ~ 5 -m footprints and 10-cm vertical precision for the Lunar Orbiter Laser Altimeter (LOLA, Smith et al. 2010a); 320×160 m field-of-view for the Diviner Lunar Radiometer Experiment (DLRE, Paige et al. 2010); 30-m zoom resolution for the Miniature Radio Frequency Technology Demonstration (Mini-RF, Nozette et al. 2010). The LRO datasets will ultimately be combined in a single reference frame based on the LOLA-defined geodetic grid, which requires accurate and consistent trajectories for geolocation. As such, the LRO mission defined a position knowledge requirement: 50–100 m total position and 1-m radially (Vondrak et al. 2010).

Our goal is to report on the current status of the LRO precision orbit determination (POD). To determine precision orbits, the LRO trajectory from 13 July 2009 to 31 January 2011 was reconstructed continuously, except for short gaps near spacecraft maneuvers. As described below, the quality of the orbits is assessed primarily through overlap analysis, i.e., the consistency of trajectory segments when processed in two consecutive time periods.

To obtain the most precise orbits for LRO, we have developed a gravity model based on the historical tracking data (Mazarico et al. 2010) and further tuned with data from LRO. This intermediary model is not optimized for geophysical purposes and is intended to be used only to improve the LRO position knowledge. The upcoming Gravity Recovery and Interior Laboratory (GRAIL) mission (Zuber et al. 2011), scheduled for launch in September 2011, should provide a lunar gravity field with far greater accuracy than what is possible to achieve from analysis of LRO tracking data.

1.2 Previous work

In the recent era of lunar exploration, the Clementine spacecraft was the first to provide the data to determine the Moon's gravity field to relatively high spatial resolutions ($l = 70$, Lemoine et al. 1997). The subsequent Lunar Prospector, with its lower orbit, in particular during the extended mission (< 50 km), enabled features as small as ~ 40 km ($l = 150 - 165$) to be resolved (Konopliv et al. 2001). The recent JAXA SELENE mission consisted of three spacecraft: the main orbiter Kaguya, in a 100 km-altitude circular orbit, and two sub-satellites which participated in a VLBI experiment. One of those sub-satellites also provided relay capability for the radio signals, between ground stations and the main orbiter. This enabled radiometric tracking of the far-side for the first time and led to great improvements in the determination of the lunar farside gravity field (Namiki 2009; Matsumoto et al. 2010; Goossens et al. 2011).

1.3 Overview

After a brief summary of the LRO mission as it relates to the presented work, we describe the tracking data types used here: radiometric Doppler and range, and altimetric crossovers from LOLA. The orbit determination process is then described in detail, followed by a discussion of the various steps in the current-best orbit reconstruction: radiometric-only orbits, the addition of the altimeter data, and the inversion of a new LRO-tuned gravity field (LLGM-1, LRO Lunar Gravity Model), which is used to converge the final trajectory. Finally, orbit overlap analyses are supplemented by results using independent data: LOLA topographic maps of the polar regions and LROC calibration information.

2 Data

2.1 Mission summary

The LRO spacecraft was launched at 22:32 UTC on 18 June 2009 from Cape Canaveral Launch Complex 41, and entered lunar orbit on 23 June 2009. Five maneuvers designed to gradually circularize the initial eccentric orbit followed, and

the spacecraft commissioning phase was initiated on 27 June 2009. The commissioning orbit was a quasi-frozen $\sim 30 \times 200$ km polar orbit ($i \sim 90^\circ$), with its periapsis near the lunar south pole.

The instrument commissioning phase began on 3 July 2009. LOLA was initially turned on for 2 days at that time and started continuous data collection on 13 July 2009. Since then, it has operated continuously except for the monthly station-keeping (SK) maneuvers, and a February 2010 safehold event.

On 15 September 2009, the spacecraft transitioned to its nominal 2-h period mapping orbit, with lower eccentricity and an average altitude of 50 km. Because of gravitational perturbations, the orbit eccentricity and argument of periapsis naturally evolve, and monthly station-keeping maneuvers are necessary to preserve the mapping orbit (Houghton et al. 2007). The eccentricity is 0.0054 ± 0.0019 , and never more than 0.010, with the spacecraft altitude generally between 35 and 65 km (referenced to a 1,737.4 km sphere). After 1 year of the nominal Exploration mission, dedicated to the survey of the polar regions and of 50 sites selected for NASA's Constellation human space flight program, the LRO mission was extended for 2 years by the NASA Science Mission Directorate and began its Science mission.

In addition to the monthly SK maneuvers, smaller angular momentum desaturation events (δH) generally occur twice a month: once just before an SK maneuver, and the other about 2 weeks later. When the Sun-orbit geometry is favorable (large β angle¹), enough power can be generated with the solar panel held fixed, which reduces the angular momentum accumulated in the reaction wheels and can allow a δH to be skipped (e.g., in July 2010).

Other kinds of maneuvers are less frequent (yaw flip every 6 months, at $\beta \sim 0^\circ$ to keep the single solar panel oriented towards the Sun), or unique (phasing maneuver to observe the LCROSS impact in October 2009). Table S1 lists the maneuvers of the nominal and science missions.

The orbital maneuver plan leaves LRO in free flight for ~ 14 -day periods, which is desirable for orbit determination and gravity field estimation. It enables orbit reconstruction to be executed over extended time spans, thereby facilitating the recovery of long-period perturbations due to the long wavelengths of the gravity field (i.e., low-degree spherical harmonic expansion coefficients, especially the zonal and resonant terms). It also improves the contribution of altimetric crossovers to the solution, by reducing the number of effectively independent spacecraft initial states that need to be estimated.

The regularity of the spacecraft SK maneuvers leads to a natural partition of the mission into monthly periods,

¹ The beta angle (β) is the viewing angle of the Sun from the orbit, i.e., the angle between the orbit plane and the spacecraft–Sun vector.

or “phases”, each lasting for approximately one lunation (28 days). In the time period presented here (13 July 2009 to 31 January 2011), there are 21 phases in total. Commissioning, which lacks SK maneuvers, is divided into three phases of equivalent duration (CO_01 to CO_03). The nominal mission is split into 13 phases (NO_01 to NO_13), and the currently ongoing science mission consists of 5 phases (SM_01 to SM_05), as of February 2011. Table 1 gives the temporal extent of each phase.

2.2 Data description

2.2.1 Tracking data

Radiometric tracking is the most widely used method of tracking interplanetary spacecraft, providing good measurement accuracy and high operational availability. As for the case of the Lunar Prospector (LP) spacecraft in 1998–1999, the LRO spacecraft is tracked continuously, i.e., anytime it is visible from one of the ground network stations. However, unlike LP which was tracked by the NASA Deep Space Network (DSN), LRO is tracked by a new LRO-dedicated NASA station in White Sands, New Mexico, and by the commercial Universal Space Network (USN). In Table S2, we list the station positions and their contributions to total tracking. All of those stations produce S-band Doppler and range radiometric data, but only the White Sands station handles the science data downlink (telemetry), at Ka-band frequencies. The data are corrected for tropospheric delays from meteorological data collected at the stations.

The tracking strategy and S-band tracking precision requirements (1 mm s^{-1} for the White Sands station and $1.5\text{--}3 \text{ mm s}^{-1}$ for the USN stations) were chosen because of the mission cost and the navigation positioning and prediction requirements (500-m total position), but were too large to enable the position reconstruction accuracy requirements of the final LRO products (50-m total position). For that reason, a Laser Ranging capability was added to the spacecraft, providing one-way range measurements with a precision of 5–10 cm averaged over 5 s (Zuber et al. 2010). However, the radiometric tracking performance is better than anticipated ($\sim 0.3 \text{ mm s}^{-1}$ and $\sim 0.2 \text{ m}$ for White Sands, $\sim 0.4\text{--}0.8 \text{ mm s}^{-1}$ and $\sim 0.4 \text{ m}$ for USN; Table S2), and greatly improves the achievable orbit accuracy. For this reason and because of the intricacies of the Laser Ranging data (in particular, the estimation of station and spacecraft clock and time bias parameters), early POD efforts and the results from the current work only include radiometric tracking data. The use of Laser Ranging in LRO orbit reconstruction is however a subject of active research.

The radiometric data are complicated by the presence of biases which are typically not present in DSN tracking data. The Doppler measurements are biased, which is problem-

atic because they usually provide the strongest control of the spacecraft orbit (Table S2). Early in the mission, the Doppler data collected by the White Sands station were time-biased by $1/76\text{th}$ of a second (around -13.16 ms); this was corrected on 19 October 2009. The Range data from all stations are also affected by timing biases. Although these can be rather well characterized for each station ($\sim 5 \text{ ms}$ for White Sands, and -2 to -4 ms for USN stations), they are not constant per se, and still need to be systematically estimated. Figure S1 shows the range residuals from a sample arc (converged), with and without timing bias estimation.

2.2.2 Altimetric data

When available, accurate altimetric measurements can augment the quality of the orbit reconstructions. At each intersection between two altimetry tracks (a “crossover” location), a constraint linking the height measurements made at the two epochs and the surface height change can be created. In the case of the Moon, with small-amplitude tides ($\sim 5\text{--}10 \text{ cm}$; Williams et al. 2008), no physical topographical change above the instrument noise level (10 cm) is expected, so the reconstructed altitudes of the altimetric bounce points should be identical.

Rowlands et al. (1999) used altimetric crossovers for the orbit reconstruction of the Mars Global Surveyor (MGS) spacecraft and instrument pointing offset estimation of the Mars Orbiter Laser Altimeter (MOLA; Zuber et al. 1992). A limited amount of MOLA crossover data ($\sim 21,000$ over a 25–30 day period) was used in the orbit determination of MGS and Mars gravity field inversion (Lemoine et al. 2001). A one-month simulation study of LRO (Rowlands et al. 2009) indicated that significant improvements could be obtained from LOLA’s multi-beam configuration. LRO is the first NASA lunar spacecraft to carry a laser altimeter with sufficient capabilities to allow the use of altimetric crossovers in the orbit determination process. Goossens et al. (2011) noted improvements in certain situations with the inclusion of altimetric crossovers on the SELENE spacecraft, even though the 1-Hz LALT instrument (Araki et al. 2009) has poorer spatial resolution than the 28-Hz LOLA instrument.

The Lunar Orbiter Laser Altimeter is a 10-cm-precision 28-Hz, five-beam laser altimeter, described in detail by Smith et al. (2009). At the typical 50-km altitude, the five 5-m-diameter footprints form a 25-m-radius cross, slanted by 26 degrees with respect to the direction of flight. With each laser shot, this pattern is repeated 56 m downtrack, and progressively produces five profiles, separated in the cross-track direction by 10 m. Early results were presented by Smith et al. (2010a). With its high pulse repetition rate and multi-beam capability, the instrument collects up to 140 measurements per second. As of 31 January 2011, the LOLA dataset consists of 3.42 billion valid measurements.

Table 1 For each orbital phase, we indicate: temporal extent and duration, number of radiometric data (Doppler and range; counted twice when falling in the arc overlap periods), number of LOLA ground track intersections between orbits occurring in that phases' arcs, the crossover discrepancy RMS when converged with GLGM-3 or LLGM-1

Phase	Start epoch	Stop epoch	Duration (days)	Number (Doppler)	Number (Range)	Number cross- over locations	Crossover RMS (m) GLGM-3	Crossover RMS (m) LLGM-1
CO_01	2009 JUL 13 06:25	2009 AUG 06 12:05	24.236	161,204	149,275	2,053	1.87	1.83
CO_02	2009 AUG 06 03:03	2009 AUG 31 12:10	25.380	167,009	151,553	1,655	1.69	1.69
CO_03	2009 AUG 31 12:20	2009 SEP 26 15:12	26.119	167,098	152,452	5,886	1.90	1.79
NO_01	2009 SEP 26 22:20	2009 OCT 23 14:28	26.673	154,697	142,249	13,751	1.89	1.82
NO_02	2009 OCT 23 17:23	2009 NOV 20 14:05	27.863	179,936	169,538	15,355	3.39	3.61
NO_03	2009 NOV 20 16:56	2009 DEC 17 15:55	26.957	155,290	145,532	2,402	4.23	3.76
NO_04	2009 DEC 17 21:09	2010 JAN 13 16:50	26.820	140,192	130,102	8,810	2.08	1.96
NO_05	2010 JAN 13 19:43	2010 FEB 09 15:24	26.820	165,373	154,896	1,313	4.98	4.47
NO_06	2010 FEB 09 18:19	2010 MAR 09 14:29	27.840	144,910	137,773	3,665	1.81	1.60
NO_07	2010 MAR 09 17:23	2010 APR 05 16:54	26.980	161,755	154,814	12,330	2.09	1.99
NO_08	2010 APR 05 19:49	2010 MAY 03 15:59	27.840	169,324	158,090	4,222	2.52	2.30
NO_09	2010 MAY 03 18:52	2010 MAY 30 16:25	26.897	158,230	145,290	13,391	1.53	1.34
NO_10	2010 MAY 30 19:20	2010 JUN 27 17:15	27.913	170,943	161,711	14,065	1.86	1.66
NO_11	2010 JUN 27 20:12	2010 JUL 24 15:41	26.812	173,559	164,680	10,912	1.59	1.50
NO_12	2010 JUL 24 18:50	2010 AUG 20 10:05	26.635	170,742	159,034	11,328	2.39	2.25
NO_13	2010 AUG 20 15:25	2010 SEP 16 16:05	27.028	170,928	159,284	1,908	4.22	3.99
SM_01	2010 SEP 21 00:00	2010 OCT 14 14:55	23.622	148,411	132,015	7,821	1.65	1.52
SM_02	2010 OCT 14 20:25	2010 NOV 11 12:15	27.069	176,273	163,475	13,927	1.64	1.48
SM_03	2010 NOV 11 02:15	2010 DEC 07 11:40	26.392	166,549	150,950	1,958	2.70	2.36
SM_04	2010 DEC 07 17:15	2011 JAN 03 16:30	26.969	147,037	134,987	22,663	1.74	1.62
SM_05	2011 JAN 03 20:55	2011 JAN 31 18:40	27.906	171,595	159,265	2,878	3.34	3.20
Total	2009 JUL 13 06:25	2011 JAN 31 18:40	560.773	3,421,055	3,176,965	172,293	2.43	2.27

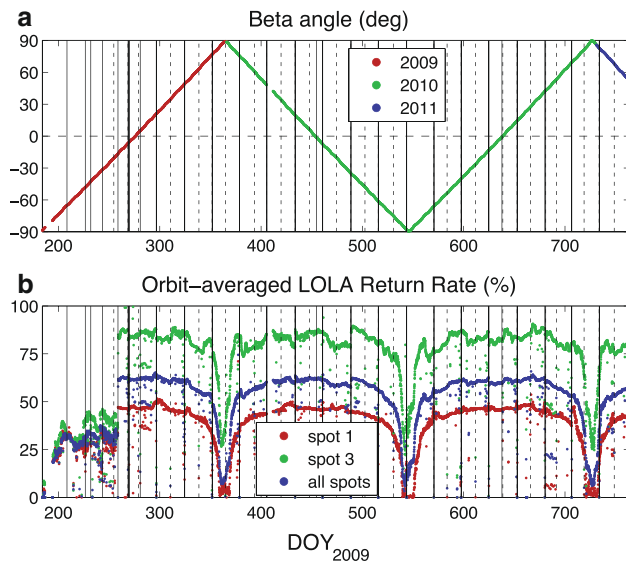


Fig. 1 **a** Time series of the β angle (in degrees) between 13 July 2009 and 31 January 2011. For reference, the δH maneuvers are indicated by a dashed line and the other maneuvers by a solid line. **b** Orbit-averaged LOLA return rates (i.e., percentage of ground returns) for spot 1, spot 3 and the 5 spots combined. Returns for spots 2 and 5 are similar to spot 1; spot 4 follows spot 3 closely. The early lower return rates are due to the eccentric commissioning orbit, when LRO was flying high over the northern hemisphere. Later, the repeated dips are correlated with high β angle values, when the spacecraft is always near the terminator, and are the result of the ‘LOLA anomaly’

Compared to the MOLA data on Mars (Zuber et al. 1992; Smith et al. 2001), with its single-beam 160-m-diameter footprints spaced by ~ 300 m, the higher resolution of the LOLA measurements improves the coverage around the groundtrack intersections, enabling more numerous (up to 25 effective crossovers at each groundtrack intersection because of the five beams) and better-quality constraints through more reliable interpolation.

However, on the nightside, the data collection is hampered by a thermal alignment anomaly (Smith et al. 2010a). When the instrument is exposed to cold temperatures, the thermal blanket contracts pulling the laser beam expander out of alignment with the receiver telescope. The displacement is significant ($\sim 600 \mu\text{rad}$) and the laser spots move out of the detectors’ fields of view ($\sim 400 \mu\text{rad}$ in diameter). Fortunately, the displacement magnitude and direction (along the Y-axis in the LOLA frame) combine to pull the transmitted laser beams 2 and 5 into the fields of view 3 and 4, so that altimetric data can still be collected the majority of the time. Consequently, channels 3 and 4 show much better average return rate than the others, as illustrated in Fig. 1.

Every orbit, altimetric data cannot be collected over short periods (typically less than a minute) around the terminator crossings, i.e., at the poles. Although the data density is reduced, these important regions can still be well mapped thanks to the polar orbit convergence and changing illumina-

tion conditions with season. In periods of high β angle ($|\beta| \sim 90^\circ$), when the LRO orbit is nearly aligned with the terminator, the orbit-averaged lunar surface temperature is low, and the orbit-averaged return rate (percentage of good returns) drops dramatically (Fig. 1). However, the dependence on the β angle is very steep, and the instrument shows substantial instrument performance degradation only a few weeks per year.

The m-daily perturbations of the lunar geopotential (Kaula 1966) produce periodic perturbations in inclination; the most significant terms are the $m = 1$ to $m = 4$, with periods of 28, 14, ~ 10 , and 7 days, respectively. Over the course of a month, the peak-to-peak variations are $\sim 1.3^\circ$. These inclination changes, on an otherwise polar orbit, allow groundtracks to intersect and altimetric crossovers to be computed. Between 13 July 2009 and 31 January 2011, we found 5,007,658 crossover locations, potentially a slight overestimate given our approach (valid data segments are picked liberally to avoid missing any crossover). When the data are actually prepared, only crossovers with sufficient valid LOLA data are used to ensure the quality of the interpolation.

Figure 2a shows the distribution of those crossovers. It is very heterogeneous, with extreme polar dominance, due to the polar convergence of the LRO polar orbit: only 12, 5.7 and 3% of the crossovers occur at latitudes less than 80° , 60° and 40° , respectively. The drape-like pattern is the result of the slow rotation of the Moon and the LRO high-inclination orbit, as noted by Rowlands et al. (2009), and the four longitude bands with fewer crossovers are due to the SK maneuvers, which always occur at the same location, and lead to the repeat of those monthly patterns. Figure 2b is identical to Fig. 2a, but with a resolution of $0.25^\circ \text{ pixel}^{-1}$ instead of $2^\circ \text{ pixel}^{-1}$, which illustrates the fact that while saturating the polar regions, all the available LOLA crossovers so far only sparsely cover the equatorial regions.

There are three main consequences of the LOLA anomaly for the POD work presented here. First, the periods near $\beta = 90^\circ$ contain fewer crossovers because of the lower average return rate. This can affect the orbit reconstruction quality of certain phases, in particular NO_03, NO_10, NO_11, and SM_05. In the future, this problem could potentially be mitigated by the use of multi-month crossover constraints (discussed in Sect. 3.3).

Second, the general strength of the crossovers is reduced. Because of the slow rotation of the Moon and the polar orbit of LRO, the crossovers occur predominantly between ascending and descending tracks. Given that we process crossover data in monthly batches, this means that in most intersecting track pairs one will have been acquired on the dayside, and the other on the nightside. Thus, instead of the anticipated geometry of five profiles intersecting five others (Rowlands et al. 2009; Mazarico et al. 2010), we usually have two tracks intersecting five and only ten single-beam crossovers (the

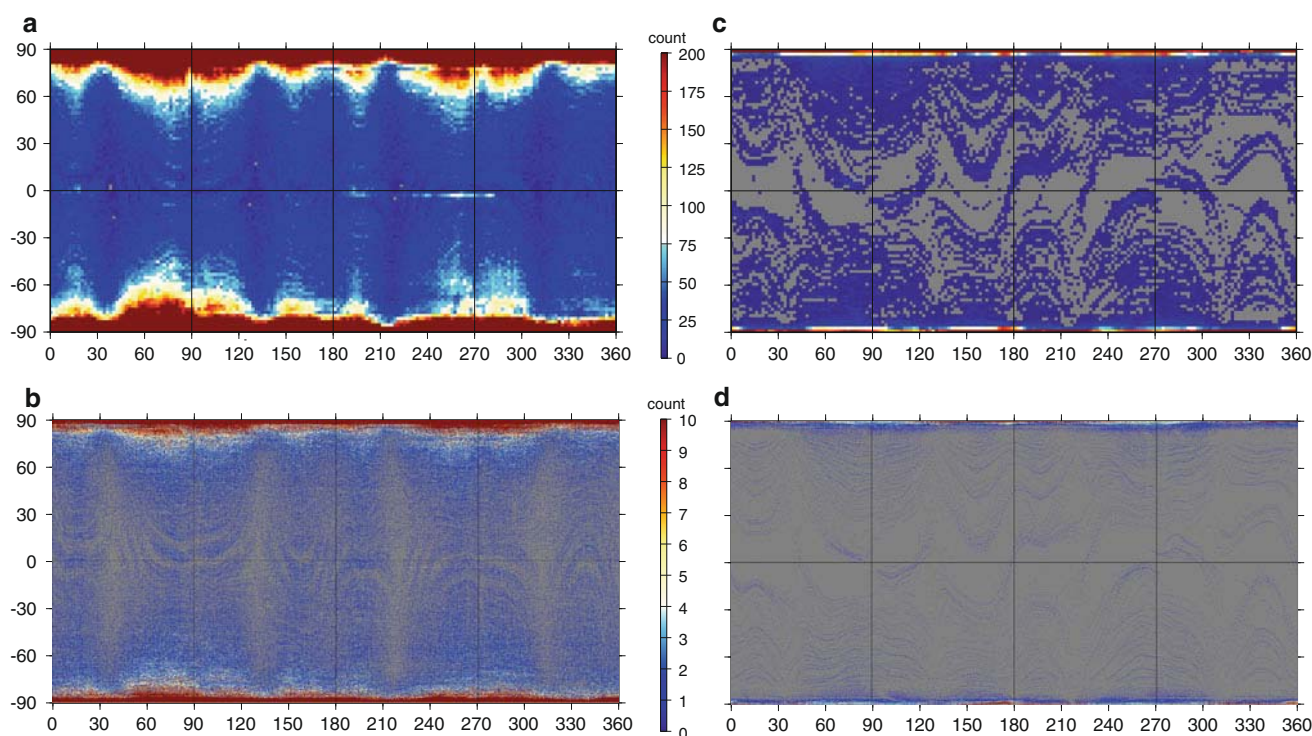


Fig. 2 Maps showing the counts of LOLA groundtrack intersections in $2 \times 2^\circ$ (a) and $0.25 \times 0.25^\circ$ (b) bins. The color scales focus on the lower counts to show the non-polar distribution. The pole values are strongly clipped, with actual count maxima of 17,929 (a) and 1,256 (b). The total count for (a) and (b) is 5,007,658. Frames (c) and (d) show similar maps, but of the counts of the LOLA crossover locations that were

actually used in the orbit determination process (i.e., only the cross-overs occurring within each phase). The clipping is not as pronounced, although the maxima are 1,276 (c) and 200 (d). The total count for (c) and (d) is 172,293. Frames (b) and (d) show that, although the coverage is global, the possible sampling and actual sampling are still sparse

measurement type used here, similar to the MOLA cross-overs used by Lemoine et al. 2001) are available, on average, at each crossover location.

Third, for the same reason, much less “cross-track” information is available in one of the two intersecting tracks, which significantly interferes with the recoverability of the relative geometric adjustment of both tracks. Only the (single-beam) altimetric cross-overs of the type used by Lemoine et al. (2001) with MGS/MOLA are employed, albeit more comprehensively than for MOLA and over a longer time period.

3 Modeling and analysis

3.1 Modeling

Precision orbit determination of the LRO spacecraft is performed with the GEODYN system of programs developed at NASA Goddard Space Flight Center (Pavlis et al. 2006). The spacecraft trajectory is integrated using a priori force models, with a number of model parameters estimated iteratively through batch least squares from the residuals of the observations with respect to the computed (modeled) values.

GEODYN was used in previous POD and gravity inversion work for the Moon (Lemoine et al. 1997; Mazarico et al. 2010; Matsumoto et al. 2010; Goossens et al. 2011), Mars (Rowlands et al. 1999; Lemoine et al. 2001) and Mercury (Smith et al. 2010b). Most of the supporting data, and force and measurement models are similar to those described in previous studies. The lunar orientation and ephemeris are based on the JPL DE421 ephemeris (Williams et al. 2008). We used the degree 150 GLGM-3 gravity field (Mazarico et al. 2010) as a priori. That gravity solution is the result of the reprocessing at NASA GSFC of historical lunar tracking data (Lunar Orbiters, Apollo sub-satellites, Clementine and Lunar Prospector), in preparation for the LRO orbit determination effort. The purpose was to create normal equations of the existing data for integration with the upcoming LRO data, as described in Sect. 3.3. The a priori value of the Love number k_2 is 0.027 (following Lemoine et al. 1997 who used the value determined from Lunar Laser Ranging by Williams et al. 1987). The trajectory integration is performed with a 5-s time step. To compute the non-conservative accelerations, the LRO spacecraft is modeled as a 10-plate macro-model and is oriented in space according to attitude telemetry in the form of quaternions. The self-shadowed plate areas are computed as described in Mazarico et al. (2009). The lunar

surface albedo model is based on a low-degree spherical harmonic expansion (Floberghagen et al. 1999). Planetary thermal radiation was not modeled, but its expected effect is small (a few meters, Mazarico et al. 2010) over the typical arc length. Following Mazarico et al. (2010), a constant along-track empirical acceleration is estimated to reduce the along-track orbit reconstruction error; the adjusted accelerations are small, around $-2 \pm 6 \times 10^{-10} \text{ m s}^{-2}$. The center-of-mass position with respect to the spacecraft body frame is considered variable and is computed based on the fuel mass and the orientation of the solar panel and high-gain antenna (HGA). Because the two gimbals of the LRO HGA orientation system are separated by $\sim 10 \text{ cm}$ (which is the LOLA-LR instrument precision), the HGA phase center offset is modeled by two non-juxtaposed single-axis gimbals. The laser altimeter data are modeled from the LOLA receiver telescope position, and constant roll and pitch pointing biases around the post-calibration boresight vector are estimated. The data weights were set to values several times above the intrinsic noise and residual root mean square (RMS): 1 mm s^{-1} for the radiometric Doppler, 10 m for the radiometric range, and 1 m for the altimetric crossovers.

3.2 Initial data analysis

3.2.1 Radiometric-only orbits

We process the data in several stages because the measurement types require different levels of processing effort: the radiometric data can be used readily and independently, but the altimetric crossovers, although they strengthen the solution, cannot stand on their own.

The radiometric data are divided into time periods called ‘arcs’, to be integrated and converged individually. Following previous work on Lunar Prospector (Konopliv et al. 2001; Mazarico et al. 2010), we used short arcs, with an average duration of 2.5 days. This length allows the arc to start and end with tracking passes from the higher-quality White Sands station. Although not necessary, this 8- to 12-h overlap period proves an important and consistent monitor of the orbit reconstruction quality, as discussed below. These short arcs are adapted to high-quality orbits: long enough to include three whole White Sands tracking sessions and a number of intervening USN tracking passes, but short enough to avoid the detrimental build-up of modeling-related errors. In total, we constructed 272 short arcs to fully cover the 21 analyzed phases. Figure S2 shows a typical arc distribution over 1 month.

We process the data in monthly batches, well after they have been collected. Each phase is divided into 12 to 14 short arcs, which are individually cleaned and converged. In this first step, we only use the radiometric data. The initial state (position and velocity) of the spacecraft is obtained from the

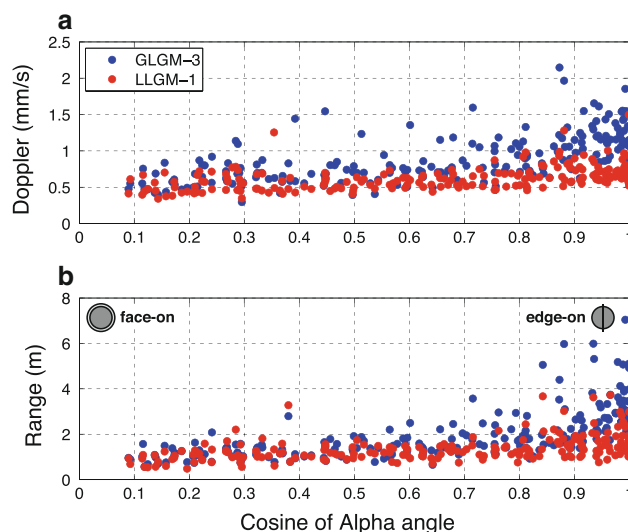


Fig. 3 Doppler (a) and range (b) residuals are plotted against the cosine of the α angle (Earth viewing angle, i.e., elevation of the Earth from the orbit plane). Face-on or edge-on (as seen from the Earth) geometries plot to the left or right, respectively. The residuals obtained after convergence with two a priori gravity fields (GLGM-3 and LLGM-1) are shown

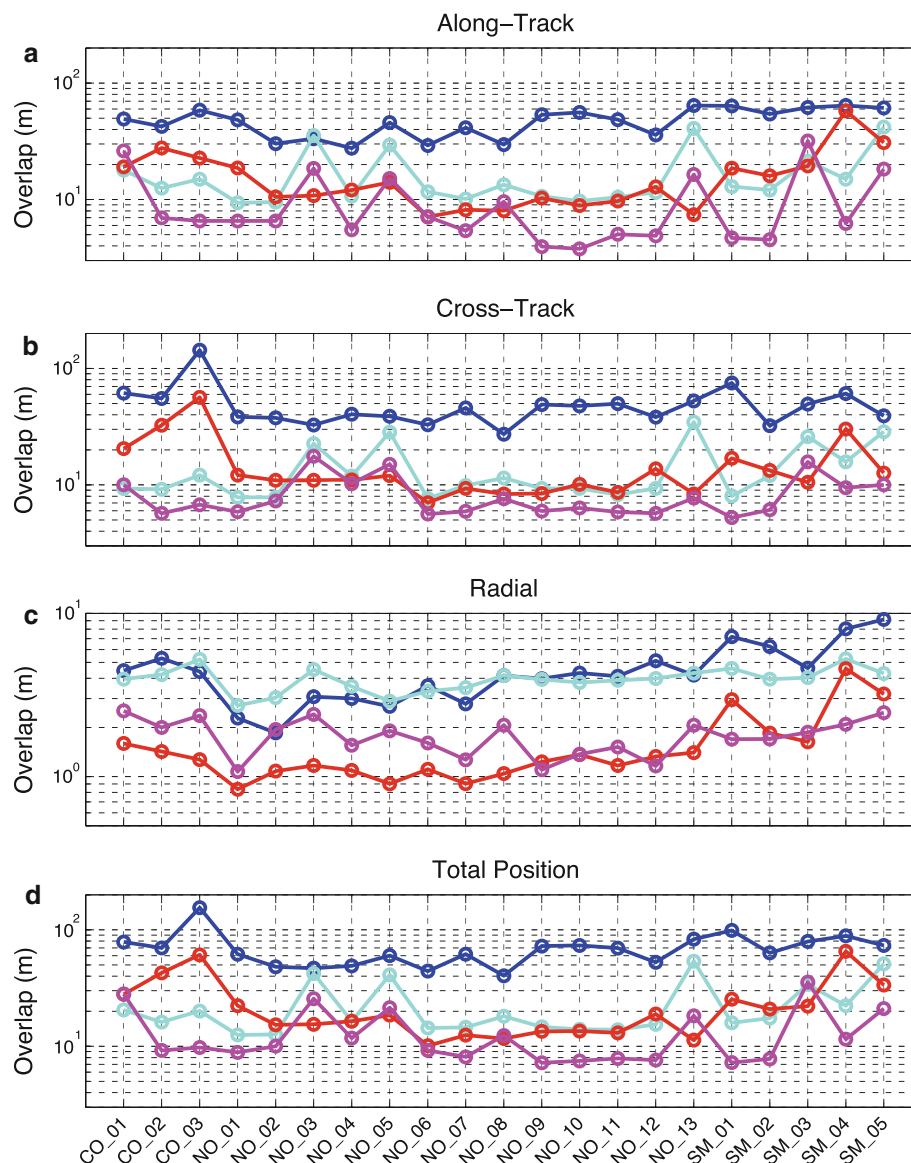
navigation team (Flight Dynamics Facility, at NASA GSFC) daily reconstructions. After a one-iteration run to manually edit out the anomalous Doppler and Range measurements, the arc is iteratively converged, by jointly estimating the values of typical arc parameters (initial state, measurement biases, radiation pressure scale factor and empirical constant along-track acceleration).

The data reduction is generally of good quality, with Doppler and range RMS values between 0.4 and 1.5 mm s^{-1} and between 1 and 4 m , respectively (Fig. 3). The arc RMS values are strongly correlated with the Earth viewing geometry angle α^2 : lower for face-on geometries ($\cos \alpha = 0$) and higher for edge-on ($\cos \alpha = 1$, when the orbit crosses the deep far side). The better fits do not indicate better orbits: when face-on, the line-of-sight direction is aligned with the horizontal component of the gravitational residual acceleration and expected to be smaller than the radial component observed in edge-on orbits.

We can assess the orbit precision (repeatability) by evaluating the RMS position difference of the trajectories computed in consecutive arc pairs during their overlapping period. This is done in the along-track (A), cross-track (C) and radial (R) directions (ACR), as well as in terms of total position (T). Over the whole period, there are 224 overlaps. (Some potential overlapping periods are voided by maneuvers.) The overlap duration is $10.5 \pm 2 \text{ h}$ (see Figure S3 for the distribution histogram).

² The alpha angle (α) is the viewing angle of the Earth from the orbit, i.e., the angle between the orbit plane and the spacecraft–Earth vector.

Fig. 4 Phase-average overlap RMS values in the along-track (a), cross-track (b) and radial (c) directions and in total position (d) for various gravity fields and data usage. Blue indicates GLGM-3 radiometric-only orbits; cyan GLGM-3 with radiometric and altimetric data. Similarly, LLGM-1 radiometric-only orbits are shown in red, and the orbits with additional altimetric crossovers in magenta



The quality of the orbits reconstructed with the radiometric data alone is close to the LRO requirements, although some periods can show larger discrepancies. In Fig. 4, we show the “phase”-averaged overlap RMS time series. Table 3 gives an overall summary of the overlap differences: 47.6 m along-track, 49.9 m cross-track, 4.5 m radial, and 70.1 m total position. The overlap RMS values calculated over each phase are presented in Table S3. In general, along-track and cross-track overlaps are smaller in edge-on and face-on geometries, respectively (Figure S4).

3.2.2 Addition of altimetric crossovers

Once all the arcs of a given phase have been converged with the radiometric data, they are ready to be combined, which

is a pre-requisite for the use of altimetric crossovers. Indeed, given the slow rotation of the Moon and the polar inclination of LRO, altimetric crossovers mostly occur between tracks ~ 14 days apart (or any multiple).

One month of individual short arcs are processed simultaneously by GEODYN, similar to the analysis of GPS data (Luthcke et al. 2003). Altimetric crossovers provide the “connection” between the separate data arcs. The ~ 28 -day duration is chosen to allow any orbit to share an altimetric crossover with another orbit, which would not be the case with a 14-day duration: only the very first and very last orbits would have crossovers. Crossover computations inevitably require non-sequential accessing of orbital information. On each iteration, the numerical integration of orbits, and associated partial derivatives, is carried out for the whole arc in advance of crossover computations, and only certain quan-

Table 2 Comparison of the values obtained by various studies for key low-degree gravitational coefficients: GM (**a**), offset by $-4.9028 \times 10^{12} \text{ m}^3 \text{ s}^{-2}$; C_{20} (**b**), offset by $+9.08938 \times 10^{-5}$; C_{21} (**c**); S_{21} (**d**); and k_{20} (**e**)

Reference	GM $- 4.9028 \times 10^{12} (\text{m}^3 \text{ s}^{-2})$	$(C_{20} + 9.08938 \times 10^{-5}) \times 10^9$	$C_{21} \times 10^9$	$S_{21} \times 10^9$	k_{20}
Dickey et al. (1994)	—	—	—	—	0.03020 ± 0.0012
Williams et al. (2009)	—	—	—	—	0.0199 ± 0.0025
Williams et al. (2011)	—	—	—	—	0.0229 ± 0.0020
LP100K	$238,000 \pm 20,600$	20.009 ± 5.319	8.383 ± 4.292	7.707 ± 0.350	n/a
LP150Q	$1,076,100 \pm 8,100$	-7.295 ± 5.348	-1.863 ± 4.409	-1.425 ± 0.335	0.0248 ± 0.0030
Goosens and Matsumoto 2008	—	—	—	—	0.0244 ± 0.0080
SGM100H	$2,121,666 \pm 13,000$	-91.596 ± 1.631	11.270 ± 1.064	-15.894 ± 1.443	0.0240 ± 0.0015
SGM100I	225,153	-102.97 ± 1.650	7.861 ± 1.045	-10.809 ± 1.349	0.0255 ± 0.0016
SGM150	795,109	6.832 ± 2.463	28.776 ± 1.534	8.248 ± 1.547	n/a
GLGM-3	238,000 (not adjusted, =LP100K)	3.654 ± 5.344	-29.620 ± 7.719	27.715 ± -4.357	0.0235 ± 0.0020
LLGM-1	$105,594 \pm 9,980$	5.102 ± 1.916	-52.865 ± 1.330	-13.345 ± 1.570	0.0270 ± 0.0004

References are given in the text. The uncertainties quoted are the 1-sigma values, except for k_{20} where we report ten times the spacecraft-derived formal errors following Konopliv et al. (2001) and Matsumoto et al. (2010)

ties from the integration are stored in memory. This way, a balance is struck between memory requirements and the computational requirements associated with non-sequential accessing of orbital information.

Because of the LOLA anomaly, we know that the laser altimeter alignment changes significantly between the day-side and the night-side, and that it varies rapidly near the terminator. However, little data are collected during those short transition times (Sect. 2.2.2), which makes it difficult to characterize the alignment other than by constant offsets from the nominally calibrated pointing. Thus, two independent sets of altimeter pointing biases (in roll and pitch) are estimated: one for the five daytime spots, and another for the two nighttime spots. Because of the large disparity in crossover temporal density, the adjusted values are really reliable only when estimated once a month (i.e., the same adjustment applied to all the arcs).

With the multi-satellite approach outlined above, we are restricted to a narrow subset of the ~ 5 million LOLA crossover locations at hand (Sect. 2.2.2). Because we process data in monthly batches, only the crossovers occurring within each month (“intra-month crossovers”) are available. Multi-month arcs, designed to access the more numerous “inter-month crossovers”, are possible but computationally challenging and of limited interest to orbit reconstruction work due to the diminishing return. Figure 2c, d shows the spatial distribution of the crossovers actually used. For each phase, we choose the crossovers which have enough LOLA data (for interpolation quality) and yield good adjustments, and then select the appropriate individual range measurements. Table 1 indicates the number of crossover locations available within each phase, with a strong β dependence (Sect. 2.2.2).

Out of those $\sim 172,000$ crossover locations, about $\sim 159,000$ are retained by GEODYN and contribute to the trajectory adjustment. In terms of actual measurements used, $\sim 951,000$ (single-beam) crossovers exist at those $\sim 172,000$ locations, of which $\sim 37,000$ are rejected during convergence. Editing criteria are high RMS of polynomial fit to the topography, high-slope terrain, large altitude discrepancy between the two tracks and sensitivity with respect to the arc parameters (i.e., large state partial derivatives). The dominant factor for LRO is the latter, with some crossovers inclined to disturb the trajectory too much compared to what we expect from the majority. Compared to the MOLA analysis (Lemoine et al. 2001), the maximum slope was relaxed (from 0.25° to 1.0°), thanks to the shorter along-track distance between consecutive bounce points and the resulting more reliable interpolation.

After orbit adjustment, the remaining height differences (crossover discrepancies) are small and comparable to the radial direction overlap (Tables 1, 2). The overall residual RMS is ~ 2.4 m. As noted above, some months, in particular at high β angles, contain fewer crossovers than nominally possible. In those cases, the crossover measurements do not significantly help the orbital solution. Figure 5 shows the distributions of both edited and retained crossover discrepancies, for a strong phase (NO_01) and a weak phase (NO_03). Only $\sim 12\%$ of the crossovers are rejected in the first case, but $\sim 49\%$ of an already smaller number are discarded for NO_03. Nevertheless, the RMS discrepancy does not exceed 5 m (cf. Table 1). As shown in Table S3, the phase NO_03 deteriorated in along-track and radial consistency, and the crossovers provided only marginal total position improvements. This is in contrast with the spectacular enhancement

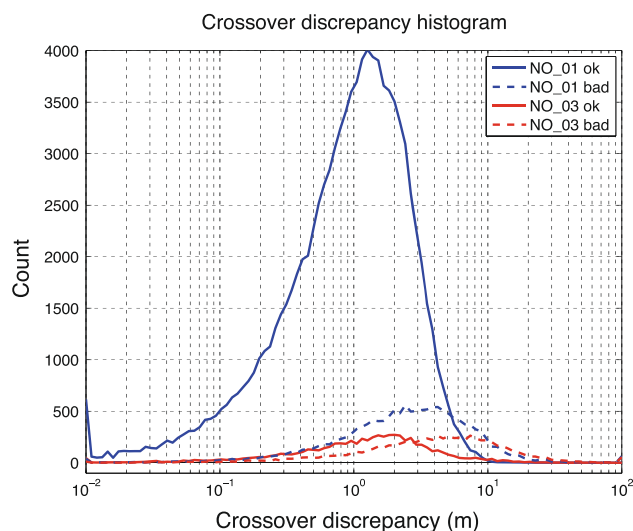


Fig. 5 Histogram of the crossover discrepancy (interpolated altitude difference at point of intersection of two LOLA spot groundtracks) for two different multi-satellite arcs: phase NO_01 (2009-09-26 to 2009-10-23, in *blue*) and phase NO_03 (2009-11-20 to 2009-12-17, in *red*). In each case, the *solid line* shows the distribution for the (single-beam) crossovers retained in the solution and the *dashed line* that of the rejected crossovers. While the strong NO_01 month has only $\sim 12\%$ of its numerous crossover measurements excluded, the NO_03 month, with already scarcer crossovers, is further weakened by the rejection of nearly half the crossover data. Note the logarithmic scale for the *horizontal axis*

observed over most orbital phases (Table S3): the overall overlap RMS values decrease from ~ 70 m in total position to ~ 23 m (Table 3), a 70% reduction.

Obviously then, the use of altimetric crossovers in the orbit determination process can help meet the LRO position knowledge requirements, also showing that they can substantially mitigate the gravity-related modeling errors.

3.3 Gravity field inversion

The natural next step is to use the signals still present in the measurement residuals to improve the gravitational force modeling. We use GEODYN to create one set of normal equations per phase and per measurement type (i.e., Doppler, range and altimetric crossover separately, which allows

re-weighting of the various measurement types during the inversion). For practical reasons, we worked only on phases CO_01 to NO_13.

Substantial changes were made to GEODYN to enable the computation of the normal equations for the crossover measurements. We mentioned above the need to pre-integrate the trajectory to use these data for orbit convergence (i.e., store the partial derivatives of the initial state and other arc parameters), but this need is exacerbated by the large number of gravitational Stokes coefficients to be estimated (22,797 for a degree-150 gravity field). We use a multi-step approach, with large temporary files to store the necessary information.

In addition, while the overlapping short arcs are important in the assessment of the orbit quality, it would be misguided to have some of the data (every other White Sands pass) counted twice in the normal equations. Instead of just truncating most of the short arcs by ~ 12 h (to remove the last White Sands pass, for example), which would make them weaker, we created an alternate set of 91 longer ~ 5 -day arcs (compared to 207 short arcs over the same time period). The quality of those arcs can of course not be assessed directly through overlap analysis, but orbit differences with the better-characterized short arcs are small. The average RMS orbit differences are 26.5, 13.5, 2.8 m in the ACR directions, and 32.8 m in total position, i.e., smaller (about half) than the short arc overlap values, giving us confidence that the longer arcs are appropriate for building normal equations.

Normal equations of the historical lunar radiometric tracking data, recently analyzed for the creation of the GLGM-3 gravity field (Mazarico et al. 2010), were recomputed with GLGM-3 as an a priori. They were then combined with the LRO normal equations and the gravity field inversion was performed. Even though our a priori weighting of the radiometric data was appropriate, the altimetric crossover data had to be downweighted, because of the large-amplitude oscillations they induced in the farside gravity field, even with the presence of a Kaula constraint. We also needed to discard the crossover normal equations of a few phases, before the obtained farside gravity field did not show excessive power (compared to GLGM-3 and SGM100i from Goossens et al. 2011). While we continue to tackle this issue, a possible

Table 3 Average overlap RMS differences, in meters, in the along-track (A), cross-track (C) and radial (R) directions, as well as in total position (T)

A priori gravity	Radio—only orbit overlaps (m)				Radio+crossover orbit overlaps (m)			
	Along	Cross	Radial	Total	Along	Cross	Radial	Total
GLGM-3 all phases	47.57	49.91	4.50	70.06	17.22	14.26	3.96	22.91
GLGM-3 NO_01 to NO_13	41.81	40.87	3.47	58.77	16.38	13.72	3.66	21.82
LLGM-1 all phases	16.71	15.44	1.58	23.39	10.18	8.37	1.80	13.63
LLGM-1 NO_01 to NO_13	10.67	10.09	1.13	14.79	8.35	8.21	1.62	12.00

For each a priori gravity field (GLGM-3 or LLGM-1), the averages are calculated over all 21 phases and over the 13 nominal phases. Results with and without the altimetric crossovers are given. More details (phase averages) are given in Tables S2 and S3

explanation is the sparsity of the crossover data of the farside (Fig. 2c-d): some data can outweigh the Kaula constraint, but are too few to yield robust estimates of the spherical harmonics expansion coefficients.

Our selected gravity field, LLGM-1 (LRO Lunar Gravity Model), is not manifestly superior than GLGM-3 in terms of geophysical performance, based on admittance and correlation studies (following Mazarico et al. 2010; not presented here). Coefficient differences between LLGM-1 and GLGM-3 are shown in Figure S5. The low-order coefficients at high degree show stronger changes compared to other high-degree coefficients. This is consistent with the LRO data affecting the determination of low-order coefficients through the m-daily perturbations. The relatively large coefficient differences in the $l = 5$ –70 band are due to a combination of the Kaula-type decrease in coefficient power with degree, and to the re-arrangement of the lumped coefficients, affected by the farside gravity field. When expanding both the GLGM-3 and LLGM-1 fields, we find that the gravity anomaly changes are small on the nearside (<10 mgal RMS excluding the polar regions) and larger on the farside, as expected (~ 62 mgal RMS). We did expect a better determination of the farside gravity anomalies thanks to the altimetric crossovers. However, in the non-polar regions, as mentioned above, the coverage by LOLA crossovers actually used in the solution is very sparse. In the polar regions (down to $\sim 70^\circ$ latitude), the lunar farside gravity field was already well characterized by the historical tracking data. However, due the great majority of LOLA crossovers occurring in that region, we see larger changes than on the nearside (~ 42 mgal RMS). Those are appreciable, although significantly smaller than the ~ 83 mgal RMS observed in the deep farside (spherical cap of half-angle 60° , centered on 180°E , 0°N). Multi-month arcs can allow us to access the complete set and potentially improve the farside gravity anomalies. This computationally intensive approach may be the subject of future work. Our goal here was to obtain a gravity solution “tuned” to LRO, with the orbital performance as metric.

Nevertheless, the addition of the LRO dataset can potentially benefit the estimation of low-degree terms in the gravitational signal, given the longer arc duration (5 days) and their links, through crossovers, over monthly timescales. Table 2 lists our estimates in comparison to previous results (Dickey et al. 1994; Williams et al. 2009, 2011; Konopliv et al. 2001; Goossens and Matsumoto 2008; Matsumoto et al. 2010; Goossens et al. 2011; Mazarico et al. 2010). The LLGM-1 adjusted values are generally consistent with the existing solutions, in particular LP100K and LP150Q (Konopliv et al. 2000, 2001), except for C_{21} and k_2 . Our C_{21} estimate is rather large and of negative sign, compared to previous estimates that were generally small and positive. Although it is not correlated with S_{21} (-0.07), the covariance matrix shows that the correlation coefficients of C_{21} with C_{30} , C_{32} and

C_{41} are rather large (0.64 , -0.79 and -0.65 , respectively). They are, however, consistently smaller than in the GLGM-3 solution, likely due to the addition of the LRO data. Our k_2 value is very close to our a priori value based on Williams et al. (1987). Other groups’ estimates are consistently lower, in the 0.023 – 0.026 range, as is our GLGM-3 adjustment (0.0235 ± 0.0002). We note however the latest SELENE estimate using VLBI (Goossens et al. 2011) data is closest to our number (0.0255 ± 0.00016). Estimates based on Lunar Laser Ranging, after a long decrease due to modeling change over the past decade (0.0302 by Dickey et al. 1994 to 0.0199 by Williams et al. 2009), have recently been revised to values more consistent with satellite-based results (0.0229 ± 0.0020 by Williams et al. 2011). The correlation of our k_2 estimate with the other low-degree coefficients is small, with a maximum (absolute) value near 0.27 with S_{30} , followed by S_{21} , C_{22} and S_{22} (smaller than 0.25). This is an improvement over GLGM-3, where the maximum correlation was 0.3 , with S_{21} .

3.4 Precise orbit reconstruction

To further improve the orbit accuracy, we reprocessed the LRO tracking data, by using the new LLGM-1 gravity field as an a priori to reprocess the short arcs. The radiometric-only arcs show improved residual Doppler and range RMS, with maxima around 1 mm s^{-1} and 4 m , respectively. This is mainly due to a better fit when the orbit is seen edge-on (Fig. 3), presumably because of a better (LRO-tuned) modeling of the integrated farside gravitational effects.

The radiometric-only orbit performance is also excellent, with dramatic improvements compared to GLGM-3 in all directions (see Fig. 4 and Table S4). The mission-averaged total position knowledge is around $\sim 23 \text{ m RMS}$ (Table 3), at the level obtained with altimetric crossovers using GLGM-3 as the a priori model. Moreover, we note that if we take the average performance over the nominal mission only, the orbit quality is further improved to $\sim 15 \text{ m RMS}$. While this could be due to the specifics of the later phases (SM_01 to SM_05), it is plausible that those latter phases would see additional improvements with a gravity solution that includes data from those phases. In other words, the overlap numbers probably reflect orbit reconstruction performance for the earlier phases and something closer to orbit prediction performance for the latter ones. This will be answered by continuing work and iterations on the LRO gravity fields.

With the inclusion of the altimetric data in the orbit convergence, similar observations can be made, but the orbit consistency is strengthened even further (Table S4). The calculated orbit overlap RMS over the whole mission are ~ 8.3 , 8.2 and 1.6 m in the along-track, cross-track and radial directions, respectively, and 12.0 m in total position. The relative improvement is much smaller than the 70% obtained with

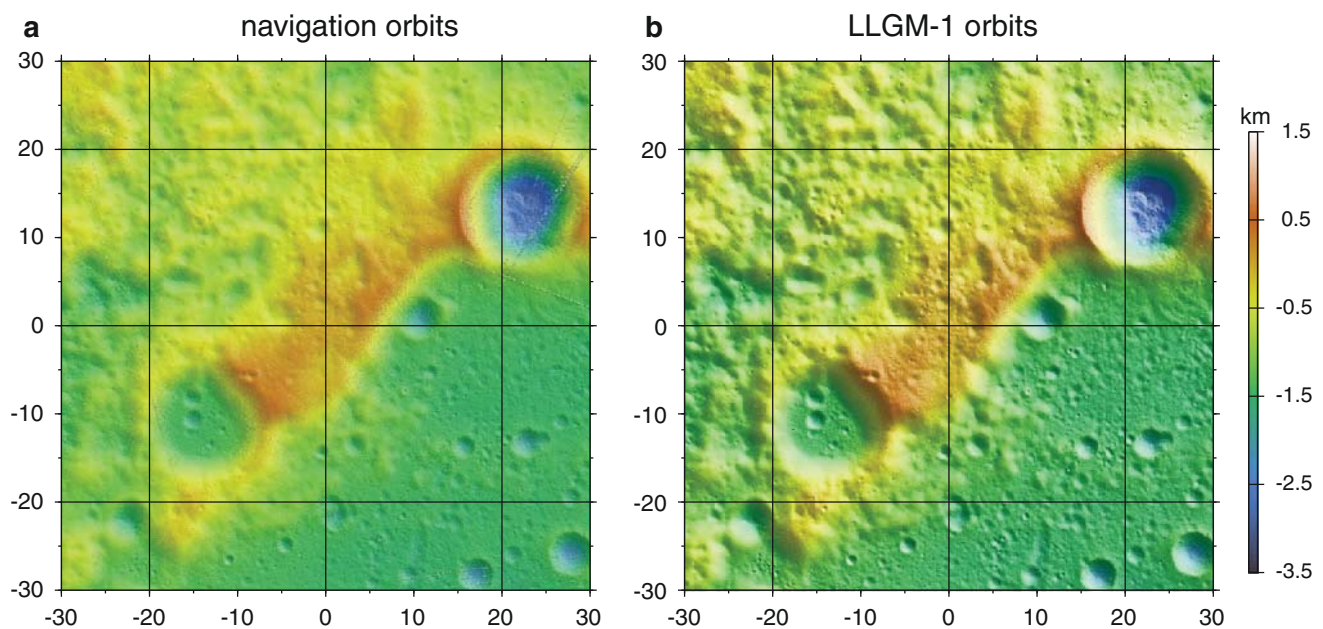


Fig. 6 Topographic maps in polar stereographic projection of the lunar north pole region (axis are in kilometers), created from LOLA data geolocated with the navigation orbits (a) and with the LLGM-1 orbits (b). The map resolution is 20 m (true scale at the pole)

GLGM-3, but still significant (19%) given the magnitude of the radiometric-only errors. The gain in the radial direction is larger (about 50%), but does not yield significantly smaller crossover discrepancies (Table 1). We note that on average the radial direction is slightly degraded by the addition of the altimetric crossovers. However, the crossover discrepancies are now commensurate with the radial overlap RMS values. The crossover residuals are smaller near the poles, where the majority of crossovers occur. The GLGM-3 overlaps were too large to observe this effect, but it was expected from the Rowlands et al. (2009) LRO simulation study: the crossovers tend to distribute the orbital errors among all directions, corrupting the empirical rule of the radial errors being ten times smaller than the horizontal errors. That rule still holds relatively well for the radiometric-only (both with GLGM-3 and LLGM-1), leading to larger radial errors when including the LOLA data. We find that the orbit differences between the radiometric-only orbits and those that include the crossovers (10.8, 7.3, 1.5 and 14.2 m on average in the ACR directions and total position, respectively) are commensurate with the differences in their overlap RMS values (Table 3), which is consistent with the crossovers bringing largely favorable orbital changes.

4 Discussion and closing remarks

4.1 Orbit accuracy assessment from independent data

The overlap analysis above shows that the LRO orbits are consistent at the 10- to 15-m level. This is technically a

measure of precision and not of the orbit accuracy itself (as required for the LRO position knowledge; Vondrak et al. 2010). The orbit accuracy is difficult to assess with the tracking measurement types we used, because the true trajectory is of course unknown. Here, we use independent data to show that the orbit precision numbers (Sects. 3.2, 3.4) are commensurate with the orbit accuracy.

Although we used a small amount of LOLA data in the POD process to construct the altimetric crossovers, the overwhelming majority of the altimetric measurements (laser bounce points) did not directly contribute to the orbit adjustment. The topographic maps produced from the complete LOLA dataset can thus be viewed as a legitimate test of the orbit accuracy, especially in the polar regions where the data density is high. In polar stereographic projection, with the orbits rotating with a monthly period, the sharpness of the topographic maps is possible only with accurate orbits.

In Fig. 6, we compare maps of the lunar north polar region (89–90° N) at 20-m resolution created with the navigation orbits (Fig. 6a) and with the orbits presented in Sect. 3.4 (Fig. 6b). Although artifacts due to orbit errors are still present in Fig. 6b, they are significantly reduced and are the result of a small number of tracks. Overall, the geolocation is excellent and broadly consistent with the overlap RMS decrease compared to other solutions (Table 3), and with the expected 20-m precision level determined from overlaps.

Images acquired with the LROC NAC camera, at 50-cm resolution, can also provide strong measures of the orbit accuracy. The LROC instrument is repeatedly pointed at the Apollo landing sites, as Constellation sites, but also as optimal calibration targets. To calibrate the instrument pointing

Table 4 Summary of the statistics of the timing residuals within LROC NAC images of the predicted and observed positions of Apollo/Lunokhod artifacts

Target	Number of observations	Timing errors (ms) navigation orbits		Timing errors (ms) LLGM-1 orbits	
		Mean	RMS	Mean	RMS
Apollo 11	10	−7.19	11.12	−2.83	6.19
Apollo 12	11	−9.98	28.58	0.44	6.13
Apollo 14	13	−6.36	12.31	−0.54	12.36
Apollo 15	11	−4.75	7.18	−5.38	6.56
Apollo 16	10	−5.16	19.61	−4.62	12.84
Apollo 17	11	−18.46	36.54	−4.40	8.96
Lunokhod 1	7	−20.52	35.21	−2.98	9.3
Average	10.4	−10.35	21.51	−2.90	8.91
Weighted average	—	−9.79	20.67	−2.81	8.96

Results with both the navigation and the LLGM-1 orbit reconstructions are given

and timing, the LROC team has been keeping track of the position of known human artifacts in the LROC NAC image frames. Those data (M.S. Robinson, personal communication) show that the orbits obtained in this work achieve improved accuracy, reducing the scatter of timing residuals (between expected and actual) from ~ 21 ms RMS to 9 ms RMS (Table 4, Figure S6). The mean of the residuals decreases significantly as well, from about -10 to -3 ms. Given the ~ 1.7 km s $^{-1}$ LRO orbital velocity, those numbers are in good agreement with the results of the overlap analysis (i.e., ~ 15 m RMS, with an average of ~ 5 m).

4.2 Creation of products and distribution

The orbits presented in Sect. 3.4 are made available as part of the LRO Radio Science PDS archive (<http://imbrium.mit.edu/LRORS/>). They are distributed as a set of SPICE kernels (Acton 1996), each spanning one of the monthly phases described in Sect. 2.1. A linear taper is used in the overlap periods to combine the trajectories of consecutive arcs. The LLGM-1 gravity field is also made available through the PDS archive or by contacting the authors.

4.3 Summary of results

In this paper, we presented the data and methods used by the LOLA POD team to reconstruct the LRO spacecraft trajectory to satisfy the LRO position knowledge requirements and to enable the geolocation and comparison of the various high-resolution datasets being acquired by the instruments onboard the spacecraft. We demonstrated through the use of overlap analysis and with the help of additional independent datasets that the orbits obtained with radiometric tracking data supplemented by LOLA-derived altimetric constraints achieve position accuracy levels around 20 m in total position

and near 1 m radially. A gravity field solution that combined pre-LRO tracking data with the newly acquired LRO geodetic measurements was developed and tuned to further improve the LRO trajectory. This resulted in accuracies better than 20 m over the whole mission (July 2009 to January 2011). This work will be continued to provide a consistent accuracy of the trajectory for all the data acquired by LRO and to establish a high-quality lunar reference frame to combine datasets of multiple spacecraft, past or future. Further enhancements can also be expected: by the creation of multi-month arcs to make use of a larger number of altimetric crossovers; and ultimately by a reprocessing of the data with a much-improved gravity field solution obtained by the GRAIL mission (Zuber et al. 2011).

Acknowledgments We thank M.S. Robinson and the LROC Science Team for providing the data used to independently validate the positioning accuracy. D. Pavlis (SGT Inc.) and C. Deng (Innovim Inc.) provided assistance with the modeling of the LRO crossover observations in GEODYN. We thank the LRO project and the flight team for the timely delivery of mission products and related information. We thank three anonymous reviewers for their thoughtful comments.

References

- Acton CH (1996) Ancillary data services of NASA's navigation and ancillary information facility. Planet Space Sci 44:65–70. doi:10.1016/0032-0633(95)00107-7
- Araki H, Tazawa S, Noda H, Ishihara Y, Goossens S, Sasaki S, Kawano N, Kamiya I, Otake H, Oberst J, Shum C (2009) Lunar global shape and polar topography derived from Kaguya-LALT laser altimetry. Science 323(5916):897–900. doi:10.1126/science.1164146
- Chin G, Brylow S, Foote M, Garvin J, Kasper J, Keller J, Litvak M, Mitrofanov M, Paige D, Raney K, Robinson M, Sanin A, Smith D, Spence H, Spudis P, Stern SA, Zuber M (2007) Lunar Reconnaissance Orbiter overview: the instrument suite and mission. Space Sci Rev. doi:10.1007/s11214-007-9153-y
- Dickey JO, Bender PL, Faller JE, Newhall XX, Ricklefs RL, Ries JG, Shelus PJ, Veillet C, Whipple AL, Wiant JR, Williams JG,

- Yoder CF (1994) Lunar laser ranging: a continuing legacy of the Apollo program. *Science* 265:482–490. doi:[10.1126/science.265.5171.482](https://doi.org/10.1126/science.265.5171.482)
- Floberghagen R, Visser P, Weischede F (1999) Lunar albedo force modeling and its effect on low lunar orbit and gravity field determination. *Adv Space Res* 23(4):733–738. doi:[10.1016/S0273-1177\(99\)00155-6](https://doi.org/10.1016/S0273-1177(99)00155-6)
- Goossens S, Matsumoto K (2008) Lunar degree 2 potential Love number determination from satellite tracking data. *Geophys Res Lett* 35:L02204. doi:[10.1029/2007GL031960](https://doi.org/10.1029/2007GL031960)
- Goossens S, Matsumoto K, Liu Q, Kikuchi F, Sato K, Hanada H, Ishihara Y, Noda H, Kawano N, Namiki N, Iwata T, Lemoine FG, Rowlands DD, Harada Y, Chen M (2011) Lunar gravity field determination using SELENE same-beam differential VLBI tracking data. *J Geod* 85(4):205–228. doi:[10.1007/s00190-010-0430-2](https://doi.org/10.1007/s00190-010-0430-2)
- Houghton MB, Tooley CR, Saylor RS Jr (2007) Mission design and operations considerations for NASA's Lunar Reconnaissance Orbiter. 58th International Astronautical Congress, Hyderabad, India. http://lunar.gsfc.nasa.gov/library/IAC-07-C1_7_06.pdf
- Kaula WM (1966) Theory of satellite geodesy. Blaisdell Publishing Co., London 124
- Konopliv AS, The Lunar Prospector Gravity Science Team (2000) LP150Q Spherical Harmonic Model. http://pds-geosciences.wustl.edu/lunar01/lp-1-rss-5-gravity-v1/lp_1001/sha/jgl150q1.sha (published 27 Nov. 2000)
- Konopliv AS, Asmar SW, Carranza E, Sjogren WL, Yuan D-N (2001) Recent gravity models as a result of the Lunar Prospector mission. *Icarus* 150:1–18. doi:[10.1006/icar.2000.6573](https://doi.org/10.1006/icar.2000.6573)
- Lemoine FG, Smith DE, Zuber MT, Neumann GA, Rowlands DD (1997) GLGM-2: a 70th degree and order Lunar Gravity Model from Clementine and historical data. *J Geophys Res* 102(E7):16339–16359. doi:[10.1029/97JE01418](https://doi.org/10.1029/97JE01418)
- Lemoine FG, Smith DE, Rowlands DD, Zuber MT, Neumann GA, Chinn DS, Pavlis DE (2001) An improved solution of the gravity field of Mars (GMM-2B) from Mars Global Surveyor. *J Geophys Res* 106:23359–23376. doi:[10.1029/2000JE001426](https://doi.org/10.1029/2000JE001426)
- Luthcke SB, Zelensky NP, Rowlands DD, Lemoine FG, Williams TA (2003) The 1-centimeter orbit: Jason-1 precise orbit determination using GPS, SLR, DORIS and altimeter data. *Mar Geod* 26(3–4):399–421. doi:[10.1080/714044529](https://doi.org/10.1080/714044529)
- Matsumoto K, Goossens S, Ishihara Y, Liu Q, Kikuchi F, Iwata T, Namiki N, Noda H, Hanada H, Kawano N, Lemoine FG, Rowlands DD (2010) An improved lunar gravity field model from SELENE and historical tracking data: revealing the farside gravity features. *J Geophys Res* 115:E06007. doi:[10.1029/2009JE003499](https://doi.org/10.1029/2009JE003499)
- Mazarico E, Zuber MT, Lemoine FG, Smith DE (2009) Effects of self-shadowing on nonconservative force modeling for mars-orbiting spacecraft. *J Spacecr Rockets* 46(3):662–669. doi:[10.2514/1.41679](https://doi.org/10.2514/1.41679)
- Mazarico E, Lemoine FG, Han S-C, Smith DE (2010) GLGM-3: a degree-150 lunar gravity model from the historical tracking data of NASA Moon orbiters. *J Geophys Res* 115:E05001. doi:[10.1029/2009JE003472](https://doi.org/10.1029/2009JE003472)
- Namiki N, Iwata T, Matsumoto K, Hanada H, Noda H, Goossens S, Ogawa M, Kawano N, Asari K, Tsuruta S, Ishihara Y, Liu Q, Kikuchi F, Ishikawa T, Sasaki S, Aoshima C, Kurosawa K, Sugita S, Takano T (2009) Farside gravity field of the Moon from four-way Doppler measurements of SELENE (Kaguya). *Science* 323:900–905. doi:[10.1126/science.1168029](https://doi.org/10.1126/science.1168029)
- Neumann GA, Mazarico E, Smith DE, Zuber MT, Gläser P (2011) Lunar Orbiter Laser Altimeter measures of slope and roughness. Lunar and Planetary Science Conference XXXII. The Woodlands, TX (abstract 2313)
- Nozette S, Spudis P, Bussey B, Jensen R, Raney K, Winters H, Lichtenberg CL, Marinelli W, Crusan J, Gates M, Robinson M (2010) The Lunar Reconnaissance Orbiter miniature radio frequency (Mini-RF) technology demonstration. *Space Sci Rev* 150:285–302. doi:[10.1007/s11214-009-9607-5](https://doi.org/10.1007/s11214-009-9607-5)
- Paige DA, Foote MC, Greenhagen BT, Schofield JT, Calcutt S, Vasavada AR, Preston DJ, Taylor FW, Allen CC, Snook KJ, Jakosky BM, Murray BC, Soderblom LA, Jau B, Loring S, Bulharowski J, Bowles NE, Thomas IR, Sullivan MT, Avis C, De Jong EM, Hartford W, McClees DJ (2010) The Lunar Reconnaissance Orbiter diviner lunar radiometer experiment. *Space Sci Rev* 150:125–160. doi:[10.1007/s11214-009-9529-2](https://doi.org/10.1007/s11214-009-9529-2)
- Pavlis DE, Poulou SG, McCarthy JJ (2006) GEODYN operations manuals. Contractor Report, SGT Inc., Greenbelt, Maryland
- Robinson MS, Brylow SM, Tschimmel M, Humm D, Lawrence SJ, Thomas PC, Denevi BW, Bowman-Cisneros E, Zerr J, Ravine MA, Caplinger MA, Ghaemi FT, Schaffner JA, Malin MC, Mahanti P, Bartels A, Anderson J, Tran TN, Eliason EM, McEwen AS, Turtle E, Jolliff BL, Hiesinger H (2010) Lunar Reconnaissance Orbiter Camera (LROC) instrument overview. *Space Sci Rev* 150:81–124. doi:[10.1007/s11214-010-9634-2](https://doi.org/10.1007/s11214-010-9634-2)
- Rowlands DD, Pavlis DE, Lemoine FG, Neumann GA, Luthcke SB (1999) The use of laser altimetry in the orbit and attitude determination of Mars Global Surveyor. *Geophys Res Lett* 26:1191–1194. doi:[10.1029/1999GL900223](https://doi.org/10.1029/1999GL900223)
- Rowlands DD, Lemoine FG, Chinn DS, Luthcke SB (2009) A simulation study of multi-beam altimetry for lunar reconnaissance orbiter and other planetary missions. *J Geod* 83(8):709–721. doi:[10.1007/s00190-008-0285-y](https://doi.org/10.1007/s00190-008-0285-y)
- Smith DE, Zuber MT, Frey HV, Garvin JB, Head JW, Muhleman DO, Pettengill GH, Phillips RJ, Solomon SC, Zwally HJ, Banerdt WB, Duxbury TC, Golombek MP, Lemoine FG, Neumann GA, Rowlands DD, Aharonson O, Ford PG, Ivanov AB, McGovern PJ, Abshire JB, Afzal RS, Sun X (2001) Mars Orbiter Laser Altimeter (MOLA): experiment summary after the first year of global mapping of Mars. *J Geophys Res* 106:23689–23722. doi:[10.1029/2000JE001364](https://doi.org/10.1029/2000JE001364)
- Smith DE, Zuber MT, Jackson GB, Cavanaugh JF, Neumann GA, Riris H, Sun X, Zellar RS, Coltharp C, Connelly J, Katz RB, Kleyner I, Liiva P, Matuszeski A, Mazarico E, McGarry J, Novo-Gradac A-M, Ott MN, Peters C, Ramos-Izquierdo LA, Ramsey L, Rowlands DD, Schmidt S, Scott VS, Shaw GB, Smith JC, Swinski J-P, Torrence MH, Unger G, Yu AW, Zagwodzki TW (2009) The Lunar Orbiter Laser Altimeter investigation on the Lunar Reconnaissance Orbiter mission. *Space Sci Rev* 150:209–241. doi:[10.1007/s11214-009-9512-y](https://doi.org/10.1007/s11214-009-9512-y)
- Smith DE, Zuber MT, Neumann GA, Lemoine FG, Mazarico E, Torrence MH, McGarry JF, Rowlands DD, Head JW, Duxbury TH, Aharonson O, Lucey PG, Robinson MS, Barnouin OS, Cavanaugh JF, Sun X, Liiva P, Mao D-D, Smith JC, Bartels AE (2010) Initial observations from the Lunar Orbiter Laser Altimeter (LOLA). *Geophys Res Lett* 37:L18204. doi:[10.1029/2010GL043751](https://doi.org/10.1029/2010GL043751)
- Smith DE, Zuber MT, Phillips RJ, Solomon SC, Neumann GA, Lemoine FG, Peale SJ, Margot J-L, Torrence MH, Talpe MJ, Head JW, Hauck SA, Johnson CL, Perry ME, Barnouin OS, McNutt RL, Oberst J (2010) The equatorial shape and gravity field of Mercury from MESSENGER flybys 1 and 2. *Icarus* 209(1):88–100. doi:[10.1016/j.icarus.2010.04.007](https://doi.org/10.1016/j.icarus.2010.04.007)
- Vondrak R, Keller J, Chin G, Garvin J (2010) Lunar Reconnaissance Orbiter (LRO): observations for lunar exploration and science. *Space Sci Rev* 150:7–22. doi:[10.1007/s11214-010-9631-5](https://doi.org/10.1007/s11214-010-9631-5)
- Williams JG, Newhall XX, Dickey JO (1987) Lunar gravitational harmonics and reflector coordinates. In: Holota P (ed) Proceedings of the international symposium on figure and dynamics of the Earth, Moon and Planets. Astronomical Institute of the Czechoslovak Academy of Sciences, Prague, pp 643–648
- Williams JG, Boggs DH, Folkner WM (2008) DE421 Lunar Orbit, Physical Librations, and Surface Coordinates. JPL Memorandum IOM 335-JW,DB,WF-20080314-001. March 14, [ftp://ssd.jpl.nasa.gov](http://ssd.jpl.nasa.gov)

- nasa.gov/pub/eph/planets/ioms/de421_moon_coord_iom.pdf,
ftp://naif.jpl.nasa.gov/pub/naif/generic_kernels/spk/planets/de421_lunar_ephemeris_and_orientation.pdf
- Williams JG, Boggs DH, Ratcliff JT (2009) A larger lunar core? In: Lunar and Planetary Science Conference XXXX, The Woodlands, TX (abstract 1452)
- Williams JG, Boggs DH, Ratcliff JT (2011) Lunar moment of inertia and love number. In: Lunar and Planetary Science Conference XXXXII, The Woodlands, TX, (abstract 2610)
- Zuber MT, Smith DE, Solomon SC, Muhleman DO, Head JW, Garvin JB, Abshire JB, Bufton JL (1992) The Mars Observer Laser Altimeter investigation. *J Geophys Res* 97:7781–7797
- Zuber MT, Smith DE, Zellar RS, Neumann GA, Sun X, Katz RB, Kleyner I, Matuszeski A, McGarry JF, Ott MN, Ramos-Izquierdo LA, Rowlands DD, Torrence MH, Zagwodzki TW (2010) The Lunar Reconnaissance Orbiter laser ranging investigation. *Space Sci Rev* 150:63–80. doi:[10.1007/s11214-009-9511-z](https://doi.org/10.1007/s11214-009-9511-z)
- Zuber MT, Smith DE, Watkins MM, Lehman DH, Hoffman TL, Asmar SW, Konopliv AS, Lemoine FG, Melosh HJK, Neumann GA, Phillips RJ, Solomon SC, Wieczorek MA, Williams JG (2011) Gravity Recovery and Interior Laboratory (GRAIL) mission and science objectives. *Space Sci Rev* (submitted)